

A comparative study of algebraic and 3DoF models for predicting performance of all electric aircraft

Chun-Sheng Wang and Joshua Brinkerhoff*

School of Engineering, University of British Columbia, Kelowna, BC V1V 1V7, Canada

Abstract

Due to the rapid advancement of battery and electric motor technologies, all electric aircraft (AEA) are quickly becoming a promising pathway for reducing the CO₂ emissions and air pollutants of small aircraft. New design tools are needed for predicting the performance of AEA. In this study, a three-degrees of freedom (3DoF) model is developed for predicting the performance of AEA under different mission profiles and electric propulsion system efficiencies. Based on a temporal integration of the equations of motion, the 3DoF model also incorporates the AEA weight, energy storage, aerodynamics, efficiency of electric propulsion system, and atmospheric conditions in its performance predictions. Additionally, two simpler and computationally cheaper algebraic models (AM) are proposed to enable rapid performance predictions at the AEA design stage. The baseline AM is based on the flight range equation under steady conditions, which is modified in the improved AM by incorporating atmospheric effects. For a 300 nautical miles range, the improved AM predicts the maximum motor power and energy consumption with relative errors less than 4% and 5% of the 3DoF model, respectively compared with 85% and 17% from the baseline AM. The design tools are used to conduct an AEA trajectory analysis under different climb profiles and motor efficiencies. The analysis reveals that if constant motor efficiency is assumed, optimization of the AEA climb profile has little effect on the total energy consumption, with the total energy consumption differing by less than 0.5%. However, when the motor efficiency is more realistically modeled as a function of motor shaft power, differences in the total energy consumed by the AEA increase, with a maximum difference of 2.8%. Since the battery energy storage is closely related to the AEA weight and cost, this finding suggests that trajectory optimization can reduce the cost, improve the performance, and accelerate the design of AEA systems.

Keywords: All electric aircraft, Flight simulation, Aircraft performance, 3DoF model, Algebraic model.

1. Introduction

Nowadays climate crisis has surfaced as one of the biggest environmental challenges facing our planet. One of the major causes of climate crisis is greenhouse gas (GHG) emissions. It is estimated that aviation emissions will annually contribute to 25% of all GHG emissions by 2050 [1]. As a result, reducing the climate footprint of the aviation industry is imperative to combat climate change and its devastating impacts on the environment. Even though biomass-derived fuels have long been considered as the primary remedy for GHG emissions reduction, they are currently limited by the high production costs [2]. In contrast, electric aircraft have increasingly become a more viable solution with the rapid development of battery technology, especially for regional short-haul flights [3].

* Corresponding author.

Email address: joshua.brinkerhoff@ubc.ca (J. Brinkerhoff).

Generally, electric aircraft falls into three broad categories: more electric aircraft (MEA), hybrid electric aircraft (HEA), and all electric aircraft (AEA) or full electric aircraft (FEA) [4]. MEA relies on electric power to operate non-propulsion systems (hydraulic, pneumatic, and actuation) but still features a conventional fuel-powered internal combustion engine (ICE) for propulsion. HEA has a hybrid power system comprised of either a battery and conventional fuel-powered ICE or a battery and hydrogen fuel cell (HFC) whereas AEA is purely powered by an electric motor from energy stored in batteries. Among these three, Kozlova et al. [1] found that AEA are the least expensive to operate in comparison to a similarly sized traditional ICE aircraft, with the AEA's operational cost per hour being over 67% cheaper due to the lower energy cost of electricity (relative to kerosene) and maintenance cost of an all-electric powertrain [1]. Historically, Schettini et al. [5] studied on-board systems for energy management of an AEA using MATLAB/Simulink. The simulation results showed up to 32% reduction of the maximum required power. Brdnik et al. [6] discussed the impacts of AEA, HEA with a battery and ICE, and HEA with a battery and HFC on GHG emissions. AEA were found to have great advantages in zero GHG emissions and noise reduction. In addition, they analyzed the flight range of AEA as a function of payload and battery specific energy or energy density using an algebraic flight range equation. It was observed that the range is limited to low specific energy of the battery. For a large size AEA with empty weight around 30 tonne or estimated maximum takeoff weight (MTOW) of 50 tonne, the range was around 400 km with a battery specific energy of 0.2 kWh/kg.

Schäfer et al. [7] assessed the energy, economic, and environmental influences of AEA. They concluded that with a battery specific energy of 0.8 and 1.6 kWh/kg, AEA could achieve a range up to 600 and 1200 nautical miles, respectively, which correspond to 50% and 80% aircraft departures worldwide. Replacing these aircraft with AEA could respectively result in a 40% and 60% reduction in NO_x emissions, and 15% and 40% in CO_2 emissions. Viswanathan and Knapp [8] explored the scaling challenge for AEA. It was claimed that the current battery technology is sufficient to support full electrification of small vertical take-off and landing aircraft with a few passengers. Nevertheless, the scale-up of the designs to power regional jets and narrow-body aircraft (e.g., Airbus A320 or Boeing 737-sized aircraft capable of 600 nm) was still beyond the reach of current battery and motor technologies. Nagy [9] reviewed the battery and motor technology for an AEA propulsion system, and highlighted that improving the efficiency of electric motor is equally important as developing battery technologies since a minor increase in motor efficiency may cause marked enhancement in AEA range and flight time. Schefer et al. [10] evaluated electrical power systems (power converters, cables, and safety switches) for an AEA with a maximum power demand of 3700 kW for short-range flights, suggesting that a DC power distribution system with a higher voltage level is more suitable for AEA than conventional AC systems.

Barzkar and Ghassemi [11] discussed the distributed propulsion system, electric propulsion, power electronics converters, electric machines, circuit breakers, and wiring harness in electrical power systems of AEA and MEA. They concluded that technical advancements in batteries and power electronic converters play a pivotal role in commercial AEA that require high thrust power. Thapa et al. [12] reviewed the impacts of aircraft on environment and the progress of AEA in battery, electric propulsion, fuselage materials, aerodynamic design, thermal management. They emphasized that electrification of aircraft is of great important to GHG reductions and pollutants elimination, but significant improvements are needed in battery specific energy, reducing aircraft weight, and adopting advanced electro-mechanical technologies. Kozlova et al. [1] investigated the flight range of AEA for different battery specific energy (0.1-0.8 kWh/kg) and electric motor specific power or power density (1.5-20 kW/kg) using the flight range equation combined with simulation decomposition. The increment in battery specific energy and motor specific power was observed to result in longer flight range while the marginal benefits diminished with improved motor specific power. Buticchi et al. [4] examined several frameworks of aircraft electrification (MEA,

HEA, and AEA). They concluded that the specific power of electrical machines and power electronics in a AEA remains another main challenge even if the battery specific energy is considered as the major limitation. MEAs were adopted in thousands of long-distance flights while the certification and commercialization of AEA was still at the early stage. Clarke and Alonso [13] presented battery lifetime (or cell capacity) modeling of AEA for servicing commuter routes using algebraic equations. For aircraft flying eight times a day and continuously operating for a year, the battery life for achievable flight missions was found to drop by as much as 45%.

In summary, the previous studies on AEA are focused on the techno-economic and environmental analysis, or electrical power systems combined with an algebraic model (AM) mainly consisting of the flight range equation or based on the steady flight assumption. To the best of the authors' knowledge, there is a lack of research on AEA performance or trajectory analysis especially involving non-steady differential models such as the three-degrees of freedom (3DoF) equations of motion [14, 15]. Although the AM is used to estimate the flight range/energy consumption, flight time/endurance, and required motor power, it cannot predict transient behaviors of AEA during each segment of a flight mission and most importantly its accuracy is limited due to the steady flight assumption. In addition, AEA differ from traditional fuel-powered aircraft, MEA, or HEA as the total weight of an AEA is constant (i.e. there is no fuel burned during flight) and the all-electric propulsion system generally outperforms ICEs [12], which may result in very different performance despite similar equations of motion. Therefore, in this study a 3DoF model is developed and compared with a baseline and improved AM for predicting the performance (energy consumption, flight time, and maximum power of electric motor) of AEA under different mission profiles and efficiencies of electric propulsion system. Besides the equations of motion, the 3DoF model incorporates the weight equations, energy equations, aerodynamics equations, efficiency model of electric propulsion system, and atmosphere model. To further improve the accuracy of AM and in turn reduce the iterations of AEA sizing, an improved AM is proposed. The improved AEA are then employed to study the relationships between flight range and battery specific energy, motor specific power, and number of passengers. Finally, the trajectory analyses are conducted for different climb profiles using the proposed 3DoF model.

2. AEA description

Among all types of aircraft, turboprops contribute to 34% of the business aviation [1]. In the present study, the full electrification of modified turboprop Cessna Caravan with a supplemental type certificate (STC) is considered. The fuel powered Cessna Caravan (STC) has a maximum take-off weight (MTOW) of 4082 kg and a maximum flight range of around 1070 nm or 1982 km. It can seat 10-14 occupants and fly at a cruise speed up to 186 ktas or 344 km/h. The detailed specifications in both imperial and SI units are listed in Table 1. After electrification, the engine and fuel tank of Cessna Caravan are replaced with electric motor and battery, respectively whereas other components such as propeller, fuselage, and wings as well as the MTOW remain unchanged. Thus, the aerodynamics performance of this AEA is same as the original aircraft. Since the MTOW is kept as a constant, any weight change in the payload or electric motor will be absorbed by that of battery.

Table 1 Specifications of Cessna Caravan.

Parameter	Value in imperial units	Value in SI units
MTOW	8000 lb	3629 kg
MTOW (STC)	9000 lb	4082 kg
Basic empty weight	4730 lb	2145 kg
Maximum payload	3,070 lb	1,393 kg
Wing Area	279 ft ²	25.96 m ²
Wingspan	52 ft	15.9 m
Maximum range	1,070 nm	1,982 km
Maximum cruise speed	186 ktas	344 km/h
Maximum operating altitude	25,000 ft	7,620 m
Maximum climb rate	1,234 fpm	6.27 m/s
Engine power rating	675 shp	503 kW

3. Performance modeling of an AEA

3.1. 3DoF based differential model

To model the performance of AEA, several aspects have to be considered such as the aircraft weight, dynamics and kinematics, aerodynamics, atmosphere, and the power and efficiency of the powertrain. The movement (dynamics and kinematics) of an AEA could be represented by a 6DoF model or a 3DoF model similar to those of a conventional aircraft [14]. The former is the most complete model because it considers both rotational and translational motion. For the present AEA that involves small aircraft rotation axes and negligible angle, the model could be approximated by a 3DoF model [15]. The 3DoF equations of motion for non-steady flight in a vertical plane over a flat earth are expressed as [14]

$$\frac{dx}{dt} = V \cos(\gamma), \quad \frac{dh}{dt} = V \sin(\gamma), \quad (1)$$

$$\frac{dV}{dt} = \frac{1}{m} [T \cos(\alpha + \varepsilon_0) - D - mg \sin(\gamma)], \quad (2)$$

$$\frac{d\gamma}{dt} = \frac{1}{mV} [T \sin(\alpha + \varepsilon_0) + L - mg \cos(\gamma)], \quad (3)$$

where x and h respectively denote the distance and altitude, V is the true air speed, γ is the flight path angle, α is angle of attack, m is the aircraft mass, T is the thrust, D is the drag, and L is the lift. ε_0 is the angle between the thrust vector and the aircraft body axis, which is generally very small. Here, ε_0 is assumed to be zero. g is the gravitational acceleration, equal to 9.81 m/s².

Different from a fuel-powered aircraft, m of an AEA is a constant during a flight mission, i.e.,

$$dm/dt = 0 \text{ or } m = \text{constant}. \quad (4)$$

m consists of the mass of airframe (m_{af}), payload (m_{pl}), battery (m_b), and motor (m_m) [16]:

$$m = m_{af} + m_{pl} + m_b + m_m . \quad (5)$$

Here, m_{af} , m_{pl} , m_b , m_m are respectively evaluated by

$$m_{af} = C_{maf}m, \quad m_b = E/\rho_{E,b}, \quad m_m = P_r/\rho_{P,m}, \quad (6a)$$

and

$$m_{pl} = N_{pax}m_{p0} + N_{crew}m_{c0} . \quad (6b)$$

C_{maf} represents the airframe weight to MTOW ratio, which is 0.54 for the present AEA. E is the total energy of the battery that is fully charged (State of charge SoC = 1) and $\rho_{E,b}$ denotes the battery specific energy. P_r is the rated output power (mechanical power or shaft power or brake horsepower or output power) of the electric motor and $\rho_{P,m}$ is the motor specific power. N_{pax} and N_{crew} are respectively the number of passengers and crews. m_{p0} denotes the mass per passenger (180 lb) and their baggage (25 lb), namely $m_{p0} = 205$ lb whereas m_{c0} is the mass per crew with no baggage allowance, which is equal to 180 lb.

The aerodynamic forces L and D are defined as

$$L = \frac{1}{2}C_L\rho SV^2, \quad D = \frac{1}{2}C_D\rho SV^2, \quad (7)$$

where C_L and C_D are the lift and drag coefficient, respectively. ρ is the density of the atmosphere at the altitude of the aircraft and S is the wing planform area. C_L is generally approximated by the following equation

$$C_L = C_L(\alpha, Ma, Re) \approx C_L(\alpha, Ma) = C_{L\alpha}(Ma)(\alpha - \alpha_{0L}). \quad (8)$$

In practice, the Reynolds number Re and Mach number Ma effects are neglected in the above equation [14]. The zero-lift angle of attack α_{0L} is around -1.5 deg and the lift-curve slope of the wing $C_{L\alpha}$ is given by

$$C_{L\alpha} = \frac{\pi AR}{1 + \sqrt{1 + (AR/2\kappa)^2[1 + \tan^2\Lambda_{hc} - Ma^2]}}. \quad (9)$$

AR denotes the aspect ratio defined as $AR = b^2/S$ where b is the wingspan. According to Table 1, $AR = 9.74$. κ is the ratio of the airfoil lift-curve slope to the theoretical value and is close to unity for most airfoils [14]. Λ_{hc} is the half-chord sweep angle. Since Λ_{hc} and Ma are small for the present AEA, $C_{L\alpha} \approx \pi AR / [1 + \sqrt{1 + (AR/2)^2}] = 5.12 \text{ rad}^{-1}$. Ma and Re are defined as

$$Ma = \frac{V}{c_s}, \quad Re = \frac{\rho V l}{\mu}, \quad (10)$$

where c_s is the speed of sound, l is the characteristic length of the airplane, and μ is the dynamic viscosity of air at the altitude of AEA. The drag coefficient or parabolic drag polar is related to C_D via

$$C_D = C_D(\alpha, Ma, Re) = C_D(C_L, Ma, Re) = C_{D,0}(Ma, Re) + K(Ma)C_L^2. \quad (11)$$

Here, $C_{D,0}$ is the zero-lift drag coefficient and K is the induced drag factor. For $Ma < 0.8$, the Mach number and Reynolds number has little effect on the drag polar [14]. Therefore, $C_{D,0}(Ma, Re) \approx C_{D,0} = \text{constant}$ and $K(Ma) = K = \text{constant}$. $C_{D,0}$ is assumed to be 0.02 based on a similar wing design [14]. For a subsonic airplane ($Ma < \text{drag divergence Mach number}$), K is given by

$$K = \frac{1}{\pi \epsilon AR (1 + 0.5 d_T / b)}. \quad (12)$$

d_T is the diameter of wing tip tank used to reduce the induced drag resulting from an end plate effect. ϵ is the Oswald's efficiency factor indicating the difference between an elliptical and straight-tapered planform, which is approximated by

$$\epsilon = (1 - 0.045AR^{0.68})(1 - 0.227\Lambda_{qc}^{1.615}). \quad (13)$$

For the present AEA, the quarter-chord sweep angle $\Lambda_{qc} \approx 1.5$ deg, thus $\epsilon \approx 0.8$. Since there are no tip tanks ($d_T = 0$), $K = 1/(\pi \epsilon AR) = 0.041$.

As the cruise altitude of the turboprop is normally in the troposphere (sea-level to 36,000 ft) as shown in Table 1, the atmospheric density, speed of sound, and dynamic viscosity can be described by [17]

$$\rho = \frac{p M_0}{T_a R_s}, \quad c_s = \sqrt{\gamma_a T_a \frac{R_s}{M_0}}, \quad \mu = \mu_0 \left(\frac{T_a}{T_{ar}} \right)^{3/2} \frac{T_{ar} + T_{as}}{T_a + T_{as}}. \quad (14)$$

M_0 is the molecular weight of air, R_s is the universal gas constant, γ_a is the adiabatic index, and the constants $\mu_0 = 1.716 \times 10^{-5}$ Pa·s, $T_{ar} = 273.11$ K, $T_{as} = 110.56$ K. T_a and p respectively denote the atmospheric temperature and pressure determined by

$$T_a = T_{a0} - T_{aL}h, \quad p = p_0 \exp \left[\frac{g_0 M_0}{R_s T_{aL}} \ln \left(\frac{T_{a0}}{T_a} \right) \right], \quad (15)$$

where $T_{a0} = 288.15$ K, $T_{aL} = 0.0065$ K/m. Combing Eq. (14) and (15), ρ can be expressed as a function of h as

$$\rho = \frac{p_0 M_0}{R_s (T_{a0} - T_{aL}h)} \exp \left[\frac{g_0 M_0}{R_s T_{aL}} \ln \left(\frac{T_{a0}}{T_{a0} - T_{aL}h} \right) \right]. \quad (16)$$

Based on T and V , the mechanical power of the motor and total energy consumption are respectively calculated by

$$P = \frac{\mathbf{T} \cdot \mathbf{V}}{\eta_p} = \frac{TV \cos(\alpha + \epsilon_0)}{\eta_p} = \frac{2\pi n_{rpm} \tau}{60}, \quad (17)$$

and

$$E = \int \frac{P}{\eta_m \eta_b} dt = \int \frac{TV \cos(\alpha + \epsilon_0)}{\eta_p \eta_m \eta_b} dt. \quad (18)$$

Here, η_p , η_m , and η_b are the efficiency of propeller, efficiency of electric motor, and discharge energy efficiency of battery, respectively. n_{rpm} denotes the motor speed in round per minute (rpm) and τ is the motor torque. The maximum mechanical power of the motor is evaluated by

$$P_{max} = \max_{t \leq t_f} [P(t)], \quad (19)$$

where t_f is the flight time.

The general forms of η_p , η_m , and η_b are given by [18-20]

$$\eta_p = \eta_p(C_p, J, Ma), \quad \eta_m = \eta_m(\tau, P), \quad \eta_b = \eta_b(Cr). \quad (20)$$

J is the advance ratio defined as $J = V/(n_{rps}D_p)$ and C_p is the power coefficient defined by $C_p = P/(\rho n_{rps}^3 D_p^5)$, where D_p is the propeller tip diameter and n_{rps} is the propeller speed in revolutions per second (rps). Since variable-pitch capability is common to all high-performance propellers and the air compressibility effect is negligible for the Ma range [18], η_p is considered as a constant around 0.8. For standard electric motors (e.g. synchronous motors, low slip induction motors or conventional parallel winding DC motors), the operating speed (n_{rpm}) is close to a constant [19]. Thus, $\eta_m \approx \eta_m(\tau) = \eta_m(P)$. Cr represents the discharge C-rate of battery [21,22]. For a two-hour flight, the average C-rate is 0.5C, which corresponds to $\eta_b \approx 0.95$ [20]. Here, the capacity and power fade of battery [13, 23] are not considered (assume first time use and battery is able to provide the required power at anytime during a flight mission). Also, the battery thermal effect [24] is neglected; the battery thermal management system is assumed to control the cell temperature to remain within a reasonable range.

3.2. Baseline algebraic model (AM)

The AM for AEA has been derived by previously [1, 10]. Here, the model will be extended to incorporate the weight of electric motor and battery discharge energy efficiency, and compared against the 3DoF model described above. For a steady cruise, $\gamma = 0$, $\cos(\alpha + \varepsilon_0) \approx 1$, and $\sin(\alpha + \varepsilon_0) \approx 0$ [14]. Thus, Eq. (3) and (4) are simplified as

$$L - mg = 0, \quad T - D = 0. \quad (21)$$

Here, the aircraft is assumed to cruises at the best lift-to-drag ratio $(L/D)_{max}$, namely

$$\frac{L}{D} = (L/D)_{max}. \quad (22)$$

$(L/D)_{max}$ is assumed to be a constant equal to 20 [1]. T can be expressed as a function of weight as

$$T = D = \frac{L}{(L/D)_{max}} = \frac{mg}{(L/D)_{max}}. \quad (23)$$

Substituting Eq. (21) into Eq. (18) and noting that $\cos(\alpha + \varepsilon_0) \approx 1$, the total energy consumption is estimated by

$$E = \frac{mg}{(L/D)_{max}\eta_p\eta_m\eta_b} \int V dt = \frac{mgR}{(L/D)_{max}\eta_p\eta_m\eta_b}. \quad (24)$$

Here, η_p , η_m , and η_b are assumed to be constant, which are equal to 0.8, 0.8, and 0.95, respectively. According to Eq. (6a), Eq. (24) can be written as

$$R = \frac{\rho_{E,b}(L/D)_{max}\eta_p\eta_m\eta_b}{g} \left(\frac{m_b}{m}\right). \quad (25)$$

Note the total energy of battery is assumed to be equal to the trip energy E since taxi energy, contingency energy, final reserve energy, alternate energy, etc., are not considered. For a constant cruise speed V_c , the flight time is expressed as

$$t_f = \frac{R}{V_c} = \frac{\rho_{E,b}(L/D)_{max}\eta_p\eta_m\eta_b}{gV_c} \left(\frac{m_b}{m}\right). \quad (26)$$

V_c is equal to the average cruise speed of turboprops, namely 380 km/h. Since the maximum required mechanical power of the electric motor generally occurs during the climb phase of AEA, a quasi-steady climb is assumed, i.e., $dV/dt \approx 0$, $d\gamma/dt \approx 0$. Thus, Eq. (3) reduces to

$$T \cos(\alpha + \varepsilon_0) \approx D + mg \sin(\gamma). \quad (27)$$

Substituting the above equation into Eq. (17) and assuming $D \approx mg/(L/D)_{max}$, the maximum mechanical power of the electric motor is estimated as

$$P_{max} \approx \frac{V}{\eta_p} \left[\frac{mg}{(L/D)_{max}} + mg \sin(\gamma) \right] \approx \frac{mg}{\eta_p} \left[\frac{V_c}{(L/D)_{max}} + V_h \right], \quad (28)$$

where V_h is the average rate of climb with an average value around 8 m/s.

3.3. Improved AM

Since the baseline AM above uses a constant air density and $(L/D)_{max}$ from previous empirical data, the accuracy is normally undesirable from our preliminary tests. Thus, an improved AM is proposed in this study, in which the density is described by Eq. (16). From Eq. (8) and Eq. (11), we have

$$\frac{L}{D} = \frac{C_L}{C_D} = \frac{C_L}{C_{D,0} + KC_L^2} = \frac{1}{\frac{C_{D,0}}{C_L} + KC_L} \leq \frac{1}{2\sqrt{C_{D,0}K}}. \quad (29)$$

Thus, the maximum lift-to-drag ratio $(L/D)_{max}^*$ is determined by

$$(L/D)_{max}^* = \frac{1}{2\sqrt{C_{D,0}K}}. \quad (30)$$

For $C_{D,0} = 0.02$ and $K = 0.041$ aforementioned, $(L/D)_{max}^* = 17.46$. Thus, the total energy consumption is modified as

$$E = \frac{mgR}{(L/D)_{max}^* \eta_p \eta_m \eta_b} = \frac{2mgR\sqrt{C_{D,0}K}}{\eta_p \eta_m \eta_b}. \quad (31)$$

Substituting Eq. (7) into Eq. (21), the cruise speed V_c^* is obtained

$$V_c^* = V_c^*(h_c) = \sqrt{\frac{2mg}{\rho(h_c)SC_L^*}}, \quad (32)$$

where h_c denotes the cruise altitude and C_L^* is the drag coefficient at the maximum lift-to-drag ratio, given by

$$C_L^* = \sqrt{C_{D,0}/K}. \quad (33)$$

Here, $C_L^* = 0.70$ for the assumed $C_{D,0}$ and K . According to Eq. (16), $\rho(h_c)$ is determined as

$$\rho(h_c) = \frac{p_0 M_0}{R_s (T_{a0} - T_{aL} h_c)} \exp \left[\frac{g_0 M_0}{R_s T_{aL}} \ln \left(\frac{T_{a0}}{T_{a0} - T_{aL} h_c} \right) \right]. \quad (34)$$

The flight time is revised as

$$t_f = \frac{R}{V_c^*} = \frac{\rho_{E,b}(L/D)_{max}^* \eta_p \eta_m \eta_b}{g V_c^*} \left(\frac{m_b}{m} \right). \quad (35)$$

To improve the model for estimating the maximum power, two methods are proposed in this study. One is to use Eq. (28) but replace $(L/D)_{max}$ and V_c with values given in Eq. (30) and (32). The other is to rederive the equation of power based on the quasi-steady climb assumption. For the first method, the maximum power is given by

$$P_{max} = \frac{mg}{\eta_p} \left[\frac{V_c^*}{(L/D)_{max}^*} + V_h^* \right], \quad (36)$$

where V_h^* is not a constant but a function of the practical flight trajectory. For the second method, assuming a quasi-steady climb, namely $dV/dt \approx 0$ and $d\gamma/dt \approx 0$, Eq. (3) and (4) reduce to

$$T \cos(\alpha + \varepsilon_0) - D - mg \sin(\gamma) \approx \frac{P \eta_p}{V} - \frac{1}{2} C_D \rho S V^2 - mg \gamma = 0, \quad (37)$$

$$T \sin(\alpha + \varepsilon_0) + L - mg \cos(\gamma) = \frac{1}{2} C_L \rho S V^2 - mg = 0. \quad (38)$$

Assuming α and γ are known and solve Eq. (37) and (38) for P , we have

$$P = \frac{C_D + C_L \gamma}{\eta_p C_L^{1.5}} \sqrt{\frac{2(mg)^3}{\rho S}} = \frac{C_{D,0} + K C_L^2 + C_L \gamma}{\eta_p C_L^{1.5}} \sqrt{\frac{2(mg)^3}{\rho S}}. \quad (39)$$

Assuming the maximum power is achieved at the beginning of climb [25], namely, $t = 0$, P_{max} is determined as

$$P_{max} = P_{max}(\alpha_0, \gamma_0) = \frac{C_{D,0} + K C_L^2(\alpha_0) + C_L(\alpha_0) \gamma_0}{\eta_p C_L^{1.5}(\alpha_0)} \sqrt{\frac{2(mg)^3}{\rho_0 S}}, \quad (40)$$

where α_0 and γ_0 are the angle of attack and flight path angle at the beginning of the climb. ρ_0 is the air density of the ground (sea level), which is equal to 1.225 kg/m³.

4. Model implementation and validation

Table 2 shows a summary of the system of equations for improved AM and 3DoF model. The 3DoF differential model is implemented in MATLAB Simulink® and the corresponding block diagram is shown in Fig. 1. The equations of motion, weight, energy, electric propulsion system efficiencies, aerodynamics, and atmosphere are respectively implemented within the trajectory subsystem, weight subsystem, performance, electric propulsion subsystem, aerodynamics subsystem, and atmosphere subsystem. In addition to these subsystems, a flight management subsystem is created to manage the reference variables (V , h , and x) and control variables (P and α) for a given flight mission profile. The control variable P and α correspond to the airplane throttle and control column that a pilot can control. Furthermore, the implemented equations are solved by a fifth order Runge–Kutta method. To ensure a converged simulation, the sensitivity of time step is tested with maximum relative errors of x , h , V , P , and E between two consecutive time steps remains below 1%.

Table 2 Summary of equations for the improved AM and 3DoF model

Equation type	Improved AM	3DoF model
Mass	$\frac{dm}{dt} = 0, \text{ or } m = \text{constant}$ $m = m_{af} + m_{pl} + m_b + m_m$ $m_{af} = C_{maf}m, \quad m_b = E/\rho_{E,b}, \quad m_m = P_r/\rho_{P,m}$ $m_{pl} = N_{pax}m_{p0} + N_{crew}m_{c0}$	
Kinematics & Momentum	$V_c^* = \sqrt{\frac{2mg}{\rho(h_c)SC_L^*}}, V_h^* = \text{constant}$ $L = mg$ $T = D = \frac{mg}{(L/D)_{max}^*}$	$\frac{dx}{dt} = V\cos(\gamma), \frac{dh}{dt} = V\sin(\gamma)$ $\frac{dV}{dt} = \frac{1}{m}[T\cos(\alpha + \varepsilon_0) - D - mg\sin(\gamma)]$ $\frac{d\gamma}{dt} = \frac{1}{mV}[T\sin(\alpha + \varepsilon_0) + L - mg\cos(\gamma)]$
Energy	$E = \frac{mgR}{(L/D)_{max}^*\eta_p\eta_m\eta_b}$ $P_{max} = \frac{mg}{\eta_p} \left[\frac{V_c^*}{(L/D)_{max}^*} + V_h^* \right] \text{ or}$ $= \frac{C_{D,0} + KC_L^2(\alpha_0) + C_L(\alpha_0)\gamma_0}{\eta_p C_L^{1.5}(\alpha_0)} \sqrt{\frac{2(mg)^3}{\rho_0 S}}$	$E = \int \frac{P}{\eta_m\eta_b} dt = \int \frac{TV\cos(\alpha + \varepsilon_0)}{\eta_p\eta_m\eta_b} dt$ $P = \frac{TV\cos(\alpha + \varepsilon_0)}{\eta_p} = \frac{2\pi n_{rpm}\tau}{60}$ $P_{max} = \max_{t \leq t_f} [P(t)]$
Electric Propulsion	$\eta_p = \text{constant}, \eta_m = \text{constant}$ $\eta_b = \text{constant}$	$\eta_p = \text{constant}, \eta_b = \text{constant}$ $\eta_m = \eta_m(\tau) = \eta_m(P) \text{ or constant}$
Aerodynamics	$L = \frac{1}{2}\rho V^2 SC_L^*, D = \frac{1}{2}\rho V^2 SC_D^*$ $(L/D)_{max}^* = \frac{1}{2\sqrt{C_{D,0}K}}$ $C_L^* = \sqrt{C_{D,0}/K}$	$L = \frac{1}{2}\rho V^2 SC_L, D = \frac{1}{2}\rho V^2 SC_D$ $C_L = C_{L\alpha}(\alpha - \alpha_{0L}), C_D = C_{D,0} + KC_L^2$ $C_{L\alpha} = \frac{\pi AR}{1 + \sqrt{1 + (AR/2\kappa)^2[1 + \tan^2\Lambda_{hc} - Ma^2]}}$ $K = \frac{1}{\pi\epsilon AR(1 + 0.5d_T/b)}$
Atmosphere	$\rho = \frac{p_0 M_0 \exp\left[\frac{g_0 M_0}{R_s T_{al}} \ln\left(\frac{T_{a0}}{T_{a0} - T_{al} h_c}\right)\right]}{R_s (T_{a0} - T_{al} h_c)}$	$\rho = \frac{p_0 M_0 \exp\left[\frac{g_0 M_0}{R_s T_{al}} \ln\left(\frac{T_{a0}}{T_{a0} - T_{al} h}\right)\right]}{R_s (T_{a0} - T_{al} h)}$

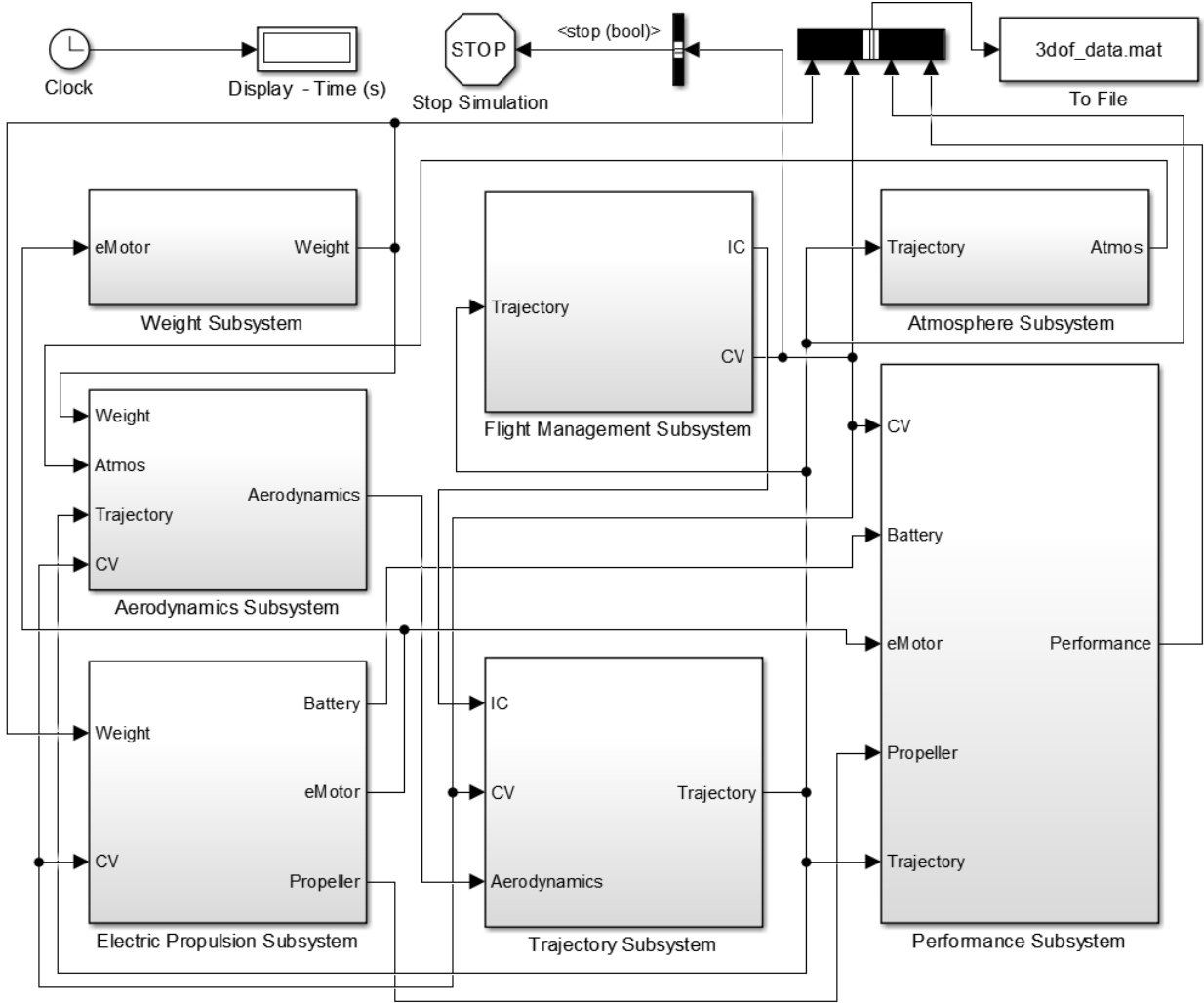


Fig. 1 Block diagram of the implemented 3DoF model in Simulink.

To validate our proposed AM, the calculated flight ranges against the airframe weight for three different payloads ($m_{pl} = 0.5, 2, 7$ tonne) are compared with those of Birdik et al. [6] as displayed in Fig. 2. Substituting Eq. (5) into Eq. (25) and neglecting the motor weight and battery heat generation (namely $\eta_b = 1$), the flight range is calculated as

$$R = \frac{\rho_{E,b}(L/D)_{max}\eta_p\eta_m}{g} \left(\frac{m - m_{af} - m_{pl}}{m} \right) = \frac{\rho_{E,b}(L/D)_{max}\eta_p\eta_m}{g} \left(1 - \frac{m_{af}}{m} - \frac{m_{pl}}{m} \right) \quad (41)$$

Note that $C_{maf} = m_{af}/m$ from Eq. (6a). Thus, the flight range with respect to m_{pl}/m_{af} is expressed as

$$R = \frac{\rho_{E,b}(L/D)_{max}\eta_p\eta_m}{g} \left(1 - C_{maf} - C_{maf} \frac{m_{pl}}{m_{af}} \right) \quad (42)$$

Here, $C_{maf} \approx 0.62$ [1]. The lower bound in Fig. 2 for the same color curves denotes $\rho_{E,b} = 0.1$ kWh while the upper bound represents $\rho_{E,b} = 0.2$ kWh. It is observed that the predicted results are in good agreement with those in the previous literature. As there is a lack of transient trajectory data for AEA, the flight range

and energy consumption by AM will be adopted to verify our developed 3DoF model in the following sections.

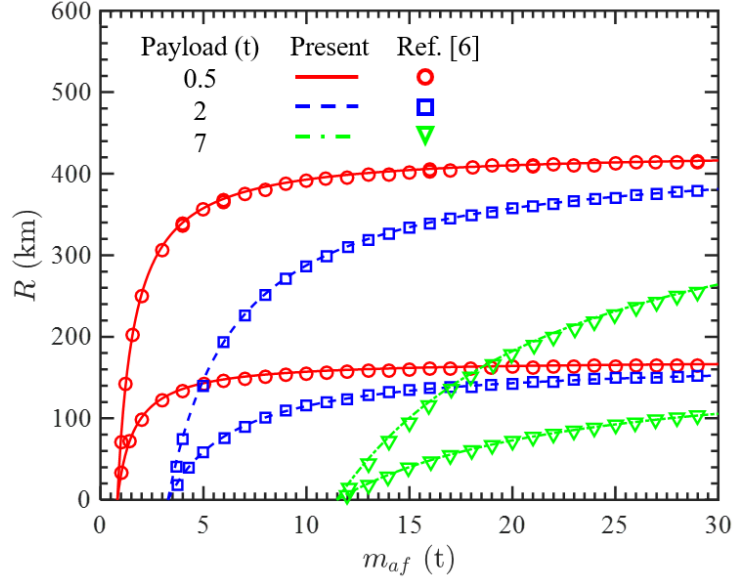


Fig. 2. Validations of the present results by algebraic model (AM) against previous data: the upper and lower curve respectively denotes a battery specific energy density of 0.1 kWh/kg and 0.2 kWh/kg.

5. Results and discussion

5.1. Comparison of models

As mentioned in Sec. 3, the AM and improved AM assume a quasi-steady flight and calculates the energy consumption based on the cruise thrust and distance. However, this assumption may not hold for AEA since the cruise distance accounts for a relatively smaller proportion of the total flying range that is limited by the specific energy density of batteries. Thus, comprehensive comparisons are made between AMs and 3DoF model to reveal the performance (assessed by the flight range R , energy consumption E , flight time t_f , and maximum motor shaft power P_{max}) difference under different mission profiles and motor efficiencies. Here, R is maintained as a constant of 300 nm or 555.6 km (a range achievable with near-term motor and battery technologies as discussed in Sec. 5.2) as it is easier to examine the effect of variable mission profiles with a fixed range. The number of passengers and crews on board are assumed to be 2 and 6, respectively. The tested mission profiles, namely MP I, II, and III, are illustrated in Fig. 3(a). These investigate the impact of cruise altitude (10,000 ft/3048 m and 20,000 ft/6096 m) and rate of climb (4 m/s and 2 m/s) on E , and t_f , and P_{max} . The rates of descent during the descent phase are similar since the minimum energy descent policy is adopted for all mission profiles. In addition, a constant and variable η_m profiles are included to show the energy consumption under ideal and practical conditions as shown in Fig. 3(b) [19], respectively. Generally, η_m of an induction DC motor depends on both speed and torque as shown in Eq. (20). As the shaft speed of the Cessna Caravan is close to a constant value, η_m is proportional to the torque or the shaft power P , namely $\eta_m = \eta_m(\tau/\tau_0) = \eta_m(P/P_0)$, where the subscript 0 denotes the cruise phase. Here η_p and η_b are assumed to be fixed considering the variable pitch technology that keeps the

optimal propeller efficiency for a wide range of advance ratios [18] and battery discharge C-rate [20]. Table 3 lists the simulated cases under different mission profiles and motor efficiency profiles.

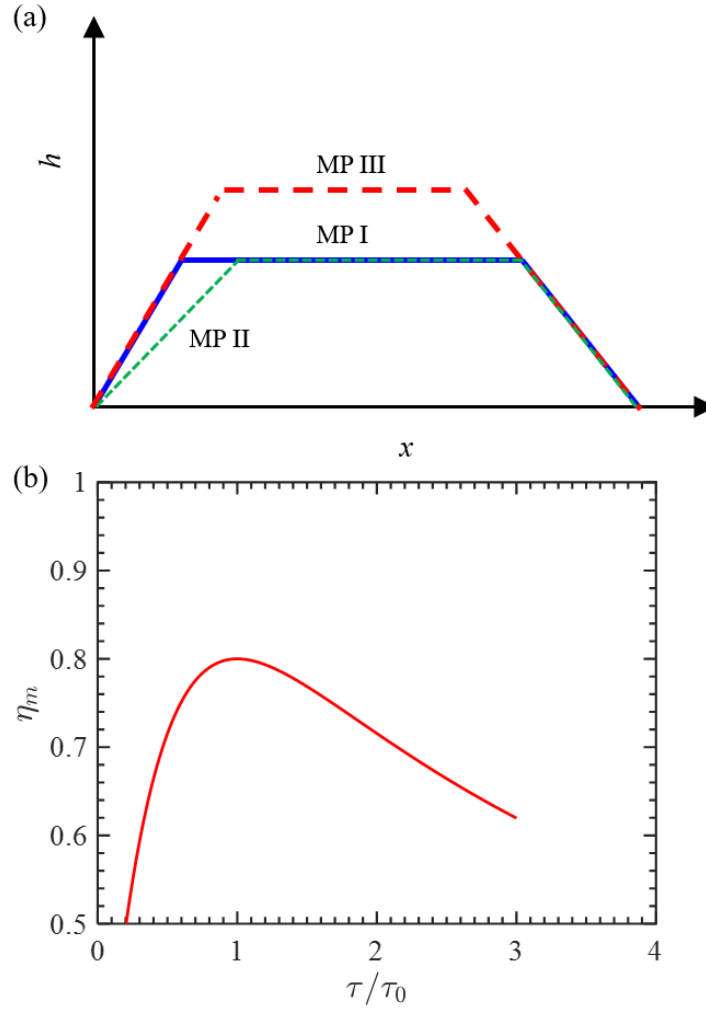


Fig. 3 (a) Mission profiles and (b) motor efficiency curve adopted for assessing AMs.

Table 3 List of studied cases for the AMs and 3DoF model.

Case no.	Mission profile	η_m	h_c (ft)
1	MP I	Constant	10,000
2	MP I	Variable	10,000
3	MP II	Constant	10,000
4	MP II	Variable	10,000
5	MP III	Constant	20,000
6	MP III	Variable	20,000

Of the studied models, only the 3DoF model accounts for the temporal variation of the AEA altitude, power, and energy consumption, which are plotted in Fig. 4 for the three mission profiles under variable η_m (case 2, 4, and 6 in Table 3). Only the cases with variable η_m are selected because the control variable P in the flight management system is derived based on the flight path angle γ and angle of attack α , resulting in similar profiles of flight distance, altitude, velocity, and power between constant and variable motor efficiency cases with the same mission profile. From Fig. 4(a), the higher cruise altitude for MP III allows for a higher cruise speed, which results in shorter flight time, but consumes more energy (Fig. 4(c)) because of the lower overall η_m . The lower rate-of-climb in MP II results in a lower maximum power at take-off (Fig. 4(b)) but does not significantly alter the total energy requirement of the flight as shown in Fig. 4(c). Table 4 displays the predicted total energy consumption E , flight duration t_f , and maximum power P_{max} from the 3DoF model as well as the baseline and improved AM. For clarity, Fig. 5 illustrates the relative error between the E and t_f values calculated by the baseline AM and improved AM in relation to those by the 3DoF model. It is obvious that the improved AM gives more accurate predictions of E and t_f for all cases than the baseline AM due to the incorporation of cruise speed and lift to drag ratio corrections. The improvements are more noticeable for t_f as it directly relates to the cruise speed which is a function of cruise altitude.

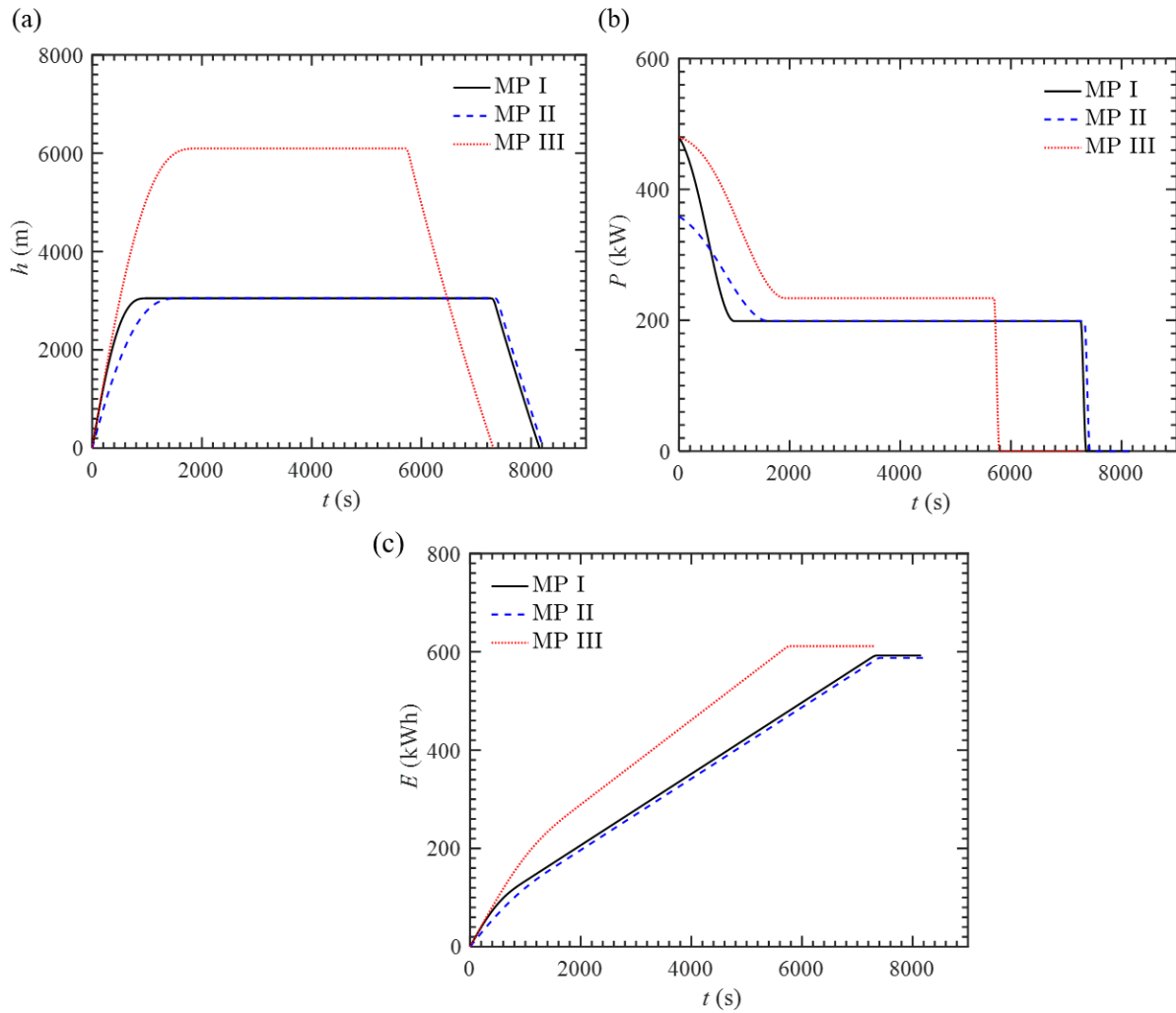


Fig. 4 (a) Altitude, (b) motor power, and (b) energy consumption versus time for three different mission profiles obtained from the 3DoF model under variable electric motor efficiency.

Table 4 Comparison of total energy consumption, flight time, and maximum motor power between AMs and 3DoF model.

Parameter	Case no.	3DoF	AM	Improved AM	
				Eq. (36)	Eq. (40)
E (kWh)	1	580.6	508.3	582.2	
	2	592.5	508.3	582.2	
	3	581.2	508.3	582.2	
	4	587.6	508.3	582.2	
	5	581.5	508.3	582.2	
	6	611.4	508.3	582.2	
t_f (s)	1	8155	5264	7951	
	2	8155	5264	7951	
	3	8222	5264	7951	
	4	8222	5264	7951	
	5	7312	5264	6756	
	6	7312	5264	6756	
P_{max} (kW)	1	479.7	664.7	400.6	498.7
	2	479.7	664.7	400.6	498.7
	3	358.7	664.7	300.4	368.9
	4	358.7	664.7	300.4	368.9
	5	479.7	664.7	436	498.7
	6	479.7	664.7	436	498.7

Overall, the maximum errors of E and t_f are less than or equal to 17% and 36% for AM, respectively, while they are 5% and 8% for the improved AM. For different η_m profiles, the errors of E with variable η_m are slightly larger than those with constant η_m for both AMs since the practical average of η_m is lower than 0.8 adopted in AMs. The differences in t_f remain unchanged with respect to η_m as t_f is not a function of η_m for a given flight range as indicated in Eq. 35. Furthermore, the average errors of E for MP III are higher than those for MP I and MP II due to the decreased average efficiency at higher altitude. The errors of t_f predicted by improved AM show a similar trend. However, those predicted by AM decreased for MP III. This is because AM underpredicts t_f in Table 4 and the flight time for MP III decreases at higher altitude due to larger cruise speed. Also, it is seen that the extra energy consumption caused by decreased motor efficiency from different trajectories (Fig. 5(c)) cannot be modeled by the AMs that are based on the steady flight assumption as shown in Fig. 4(a).

Fig. 6 shows the relative error between the AM and 3DoF in the prediction of P_{max} . The baseline AM is observed to have the largest errors up to 85%. This is ascribed to the higher rate of climb used in Eq. (28). In contrast, the improved AM with Eq. (36) underpredicts P_{max} with errors less than 16%. This is because the drag force in Eq. (36) is approximated by that of cruise phase, which is lower than the climb phase due

to higher lift coefficient in climb. The improved AM with Eq. (36) gives accurate prediction of P_{max} with maximum errors less than 4% as it is derived from the quasi-steady equations of motion during climb. The drawback is that more parameters are required such as the initial angle of attack, flight path angle, and drag

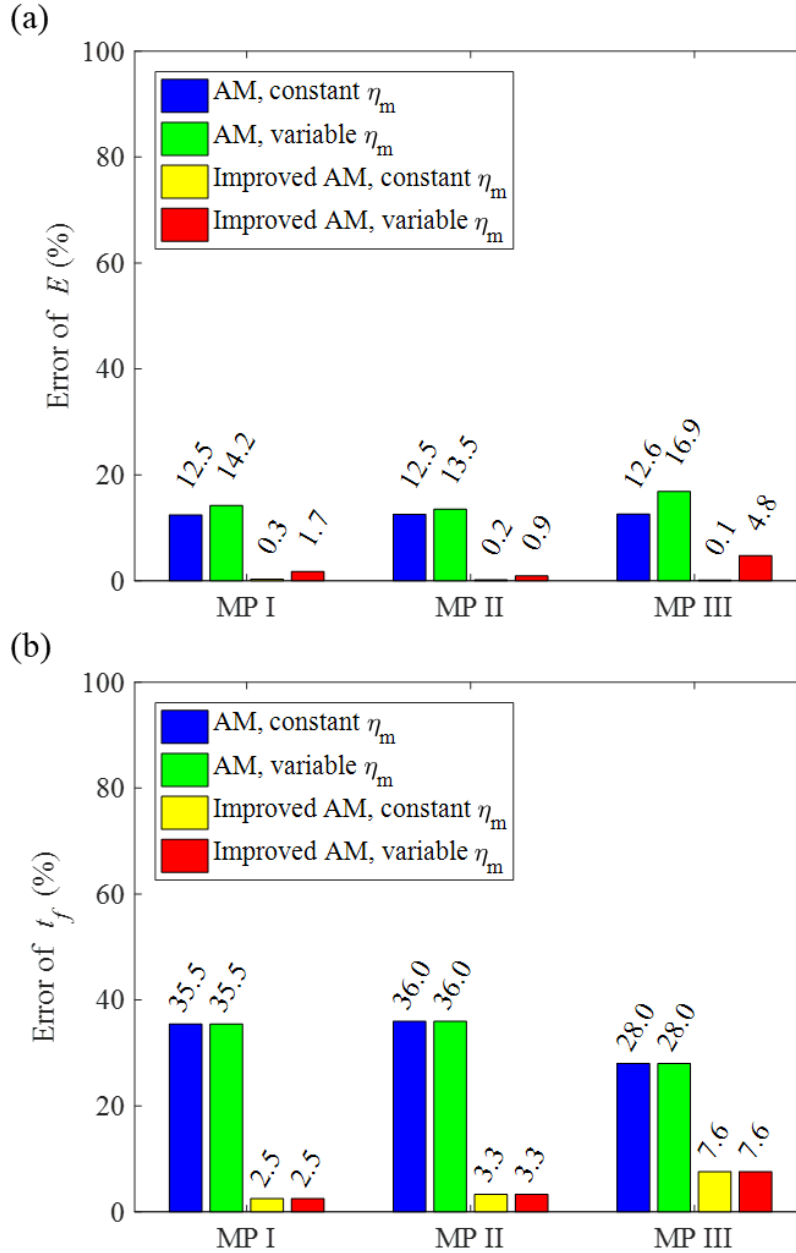


Fig. 5 Errors of (a) total energy consumption and (b) flight time by AMs relative to those by 3DoF model.

polar. As η_p is fixed to 0.8 and P is not related to η_m (Eq. (28), (36), and (40)), the error of P_{max} don't change for different η_m profiles. Nonetheless, P_{max} is sensitive to how the aircraft climb as indicated in Eq.

(28), (36), and (40) and Fig. 5(b). The lower rate of climb in MP II could cause larger deviations of P_{max} due to the assumptions made in the baseline AM Eq. (28) and improved AM Eq. (36).

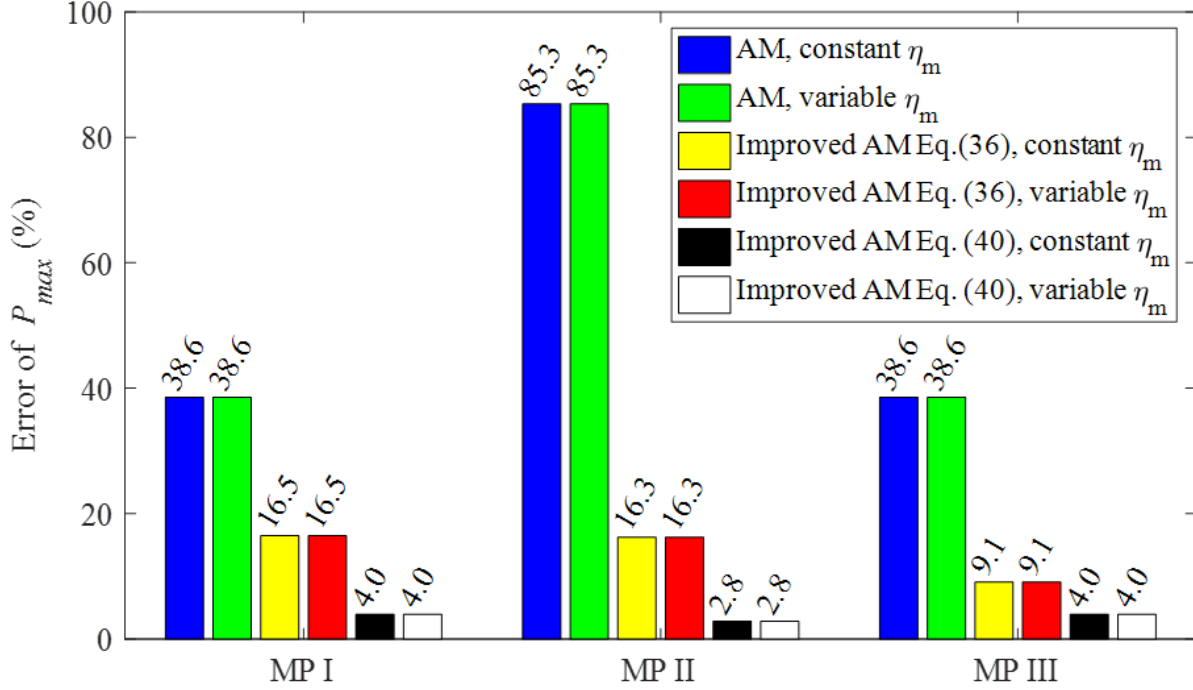


Fig. 6 Errors of maximum motor power by AMs compared with those by 3DoF model.

5.2. Flight range study

The computational cost of AMs is much lower than that of 3DoF model since it only contains only algebraic equations. Therefore, the improved AM is adopted to explore the effects of payload, $\rho_{E,b}$, and $\rho_{P,m}$ on the flight range of AEA. In this study, the payload with 6 and 9 passengers are tested considering the common number of occupants in a ICE-powered Cessna Caravan. The number of crews is fixed at 2. According to Brdnik et al. [6], the specific energy density of batteries currently available, likely achievable in the near future (next 10 years), and expected in the longer-term future (10-20 years) are in the ranges of 0.1-0.25 kWh/kg, 0.25-0.5 kWh/kg, and 0.5-0.8 kWh/kg, respectively. For the electric motor, the ranges of existing, near-term possible, and futuristic specific power are respectively 1-4 kW/kg, 4-8 kW/kg, 8-12 kW/kg. Using these value ranges within the improved AM, Fig. 7 presents the surface and contour plot of the flight range R as a function of $\rho_{E,b}$, and $\rho_{P,m}$ for 6 passengers. Obviously, R increases with both $\rho_{E,b}$, and $\rho_{P,m}$ as seen from the surface plot. The impact of $\rho_{P,m}$ on R becomes less significant for larger values. This can be explained by the relationship between R and $\rho_{E,b}$, and $\rho_{P,m}$. Substituting Eq. (5) into Eq. (25), R is expressed as a function of $\rho_{E,b}$, and $\rho_{P,m}$ as

$$R = \frac{\rho_{E,b}(L/D)_{max}\eta_p\eta_m\eta_b}{g} \left(1 - \frac{m_{af}}{m} - \frac{m_{pl}}{m} - \frac{P_r}{\rho_{P,m}} \right). \quad (43)$$

It is clear that the motor weight makes up a small portion of the total weight at higher $\rho_{E,b}$ and the saved weight for battery due to increased $\rho_{E,b}$ is negligible for larger values $\rho_{P,m}$. The maximum flight ranges for existing, near term possible, and futuristic motor and battery technology are marked on the contour plot. It is observed that the electrification of regional flights shorter than 522 km may be feasible within 10 years under the near-term battery technology scenario. The corresponding flight range distributions with 9 passengers are illustrated in Fig. 8. There is a significant drop in R and the maximum flight range for existing, near-term possible, and futuristic battery and motor technologies. From, Eq. (43), an increase in the payload causes a direct decrease in the battery weight. Thus, the flight range is very sensitive to the payload or number of passengers it can carry.

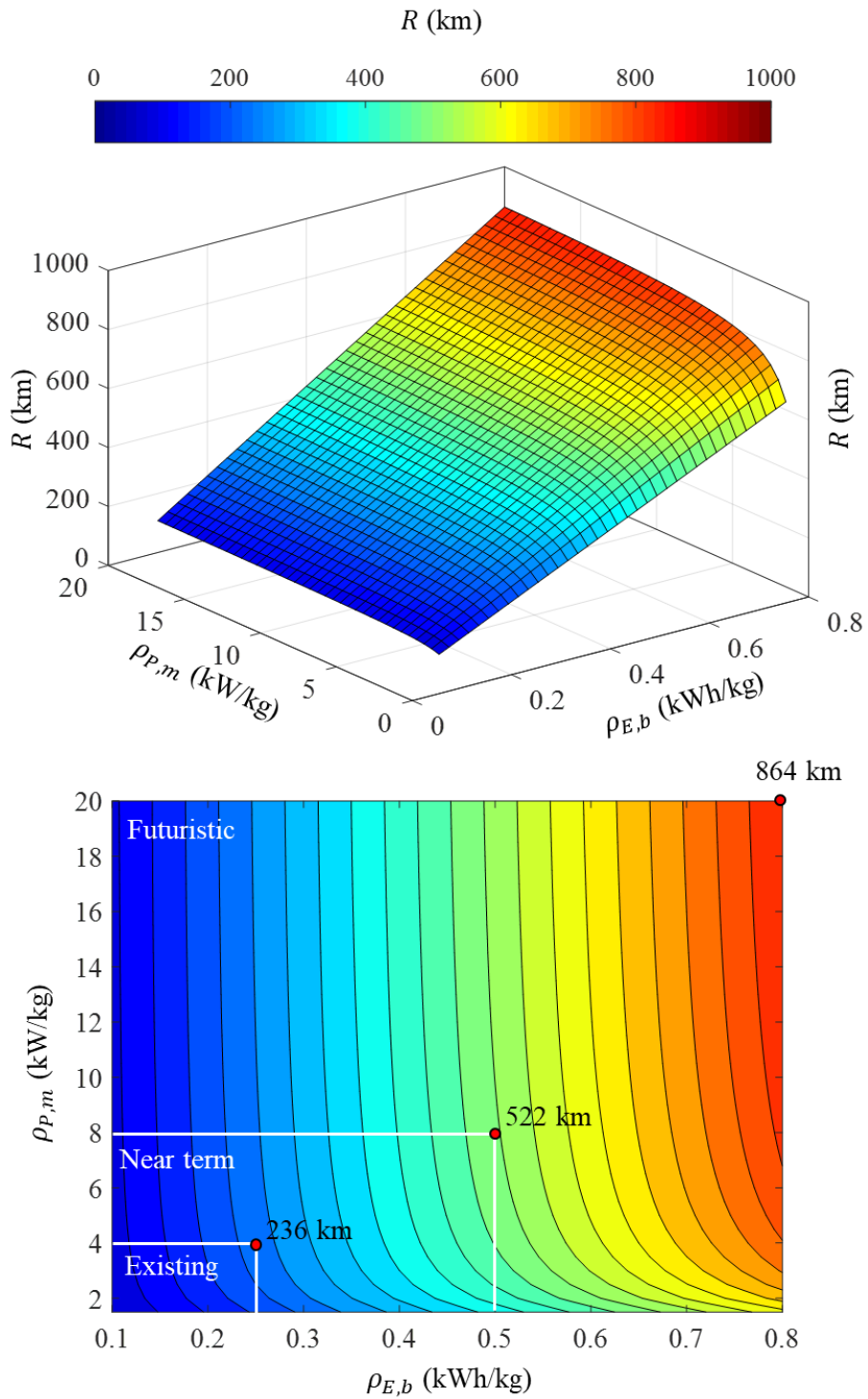


Fig. 7 Surface and contour plot of flight range as a function of battery specific energy and motor specific power for 6 passengers.

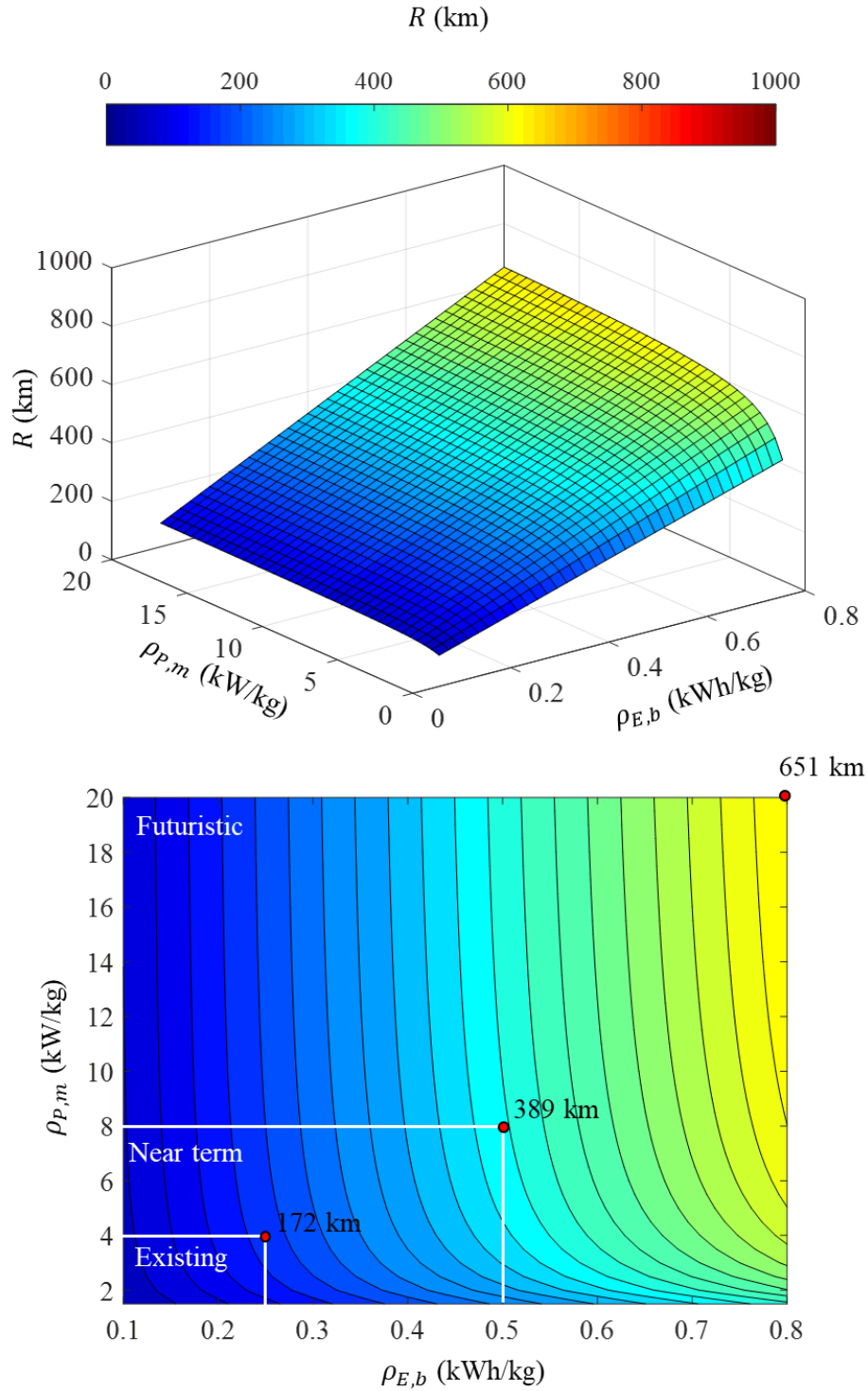


Fig. 8 Surface and contour plot of flight range as a function of battery specific energy and motor specific power for 9 passengers.

A more quantitative plot of R as a function of $\rho_{E,b}$, $\rho_{P,m}$, and number of passengers N_{pax} is displayed in Fig. 9(a), 9(b), and 9(c), respectively. Here, the upper bounds of $\rho_{E,b}$ (0.25, 0.5, and 0.8 kWh/kg) and

$\rho_{P,m}$ (4, 8, 20 kW/kg) for existing, near-term possible, and futuristic battery and motor technologies are used. The upper bound (solid lines) and lower bound (dashed lines) of the curves in Fig. 9(a) and 9(b) denotes the scenario with 6 and 9 passengers, respectively. From Fig. 9(a), R increases with $\rho_{P,m}$ but the increment is slower for larger values $\rho_{P,m}$. The trends of R with $\rho_{P,m}$ agree with those in Fig. 7 and 8. In Fig. 9(b), R is proportional to $\rho_{E,b}$ as proved in Eq. (43). For fixed MTOW, higher payload means lower battery weight as explained above. Thus, the flight range in Fig. 9(c) linearly decreases with payload.

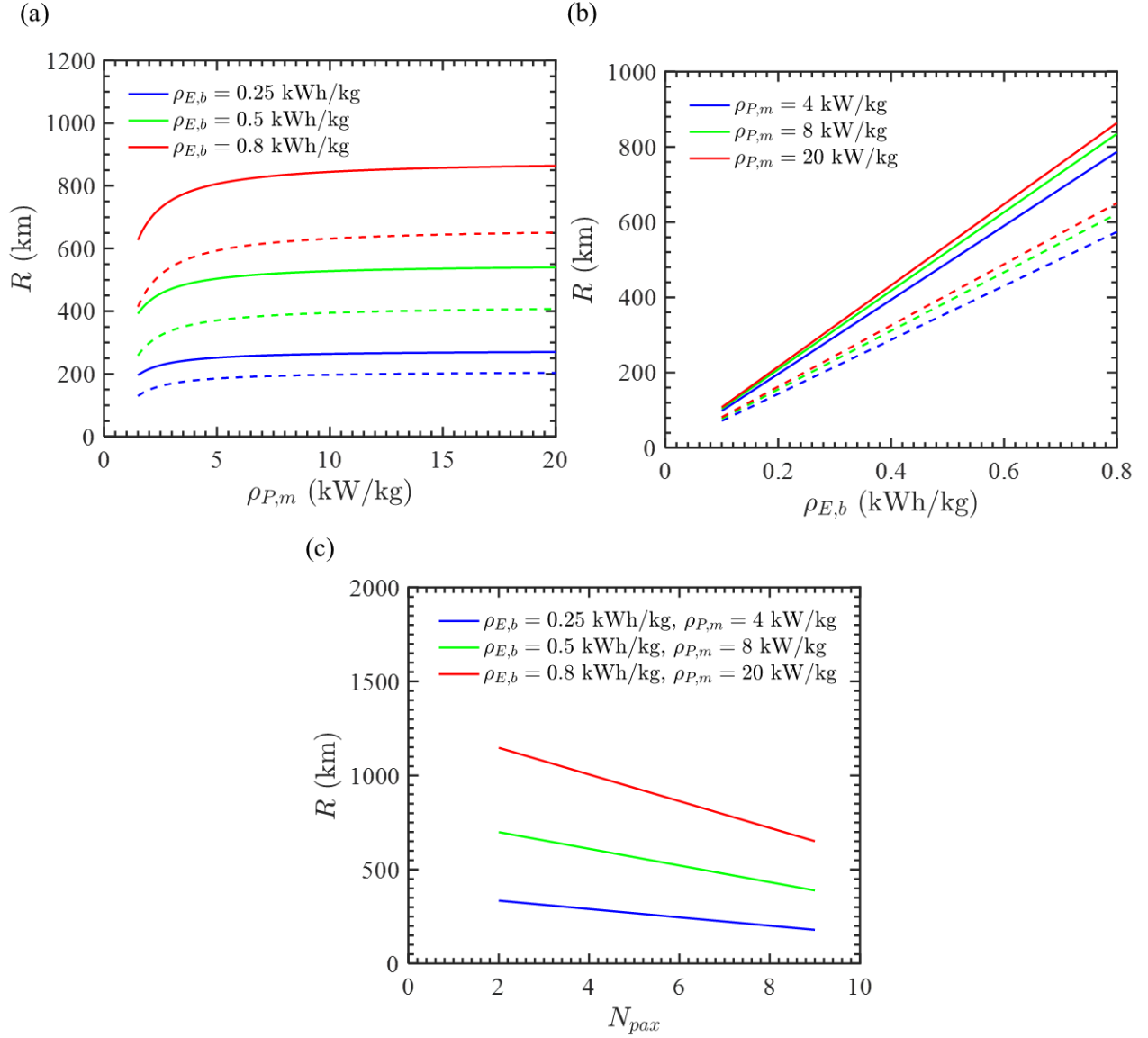


Fig. 9 Flight range as a function of (a) battery specific energy, (b) motor specific power, and (c) payload. Solid and dashed lines in (a)-(b) correspond to scenarios with 9 and 6 passengers, respectively.

5.3. Trajectory analysis

As mentioned in Sec. 5.1, the flight mission profile affects the total energy consumption. Thus, the influence of climb policies is further examined under variable or constant motor efficiencies. The three different climb profiles, namely CP I, CP II, and CP III, have for the same cruise altitude of 10,000 ft and flight range of 300 nm but different average rate of climb (3.2 m/s, 1.7 m/s, and 4.7 m/s, respectively). The climb profiles are also designed to make the control variable P a linear ($d^2P/dt^2 = 0$), convex ($d^2P/dt^2 > 0$), and concave ($d^2P/dt^2 < 0$) function of time, which are important to the calculus-of-variation based trajectory optimization in our future work. For variable motor efficiency, η_m is considered as a function of the motor torque as depicted in Fig. 3. Also, the minimum energy descent policy is used for all mission profiles and the maximum P is controlled to be less than the rated output power of motor 503 kW (Table 1). For the present 3DoF model, the control variables P and α are adjusted to achieve the different climb profiles. The simulated cases are listed in Table 5.

Table 5 List of studied cases and predicted performance factors for the 3DoF model.

Case no.	Climb profile	η_m	E (kWh)	t_f (s)	P_{max} (kW)	Average V_h (m/s)
7	CP I	Constant	580.6	8155	479.7	3.2
8	CP I	Variable	592.5	8155	479.7	3.2
9	CP II	Constant	582	8274	358.7	1.7
10	CP II	Variable	587.3	8274	358.7	1.7
11	CP III	Constant	583.1	8199	492.2	4.7
12	CP III	Variable	596.8	8199	492.2	4.7

Fig. 10 shows the angle of attack and flight path angle, altitude, and true airspeed and rate of climb versus flying time for different climb profiles. Note that P in the flight management system is derived based on the flight path angle γ and angle of attack α given in Fig. 10(a) by assuming a quasi-steady flight ($dV/dt \approx 0$ and $d\gamma/dt \approx 0$), which means that the flight distance, altitude, velocity, and power curves are the same for constant and variable motor efficiency with the same climb profile. Thus, only the data with variable motor efficiency (cases 8, 10, 12) are plotted below. The predicted altitude h versus time is plotted in Fig. 10(b). Clearly, the cruise altitude is the same and the three examined climb profiles (CP I, CP II, and CP III) have different values of average rate of climb. The differences in the climb time are noticeable since the rate of climb or vertical velocity component V_h is different as shown in Fig. 10(c). It is also noted that the true air speed V in Fig. 10(c) does not vary significantly throughout flight due to the limited differences in air densities resulting from the altitude change.

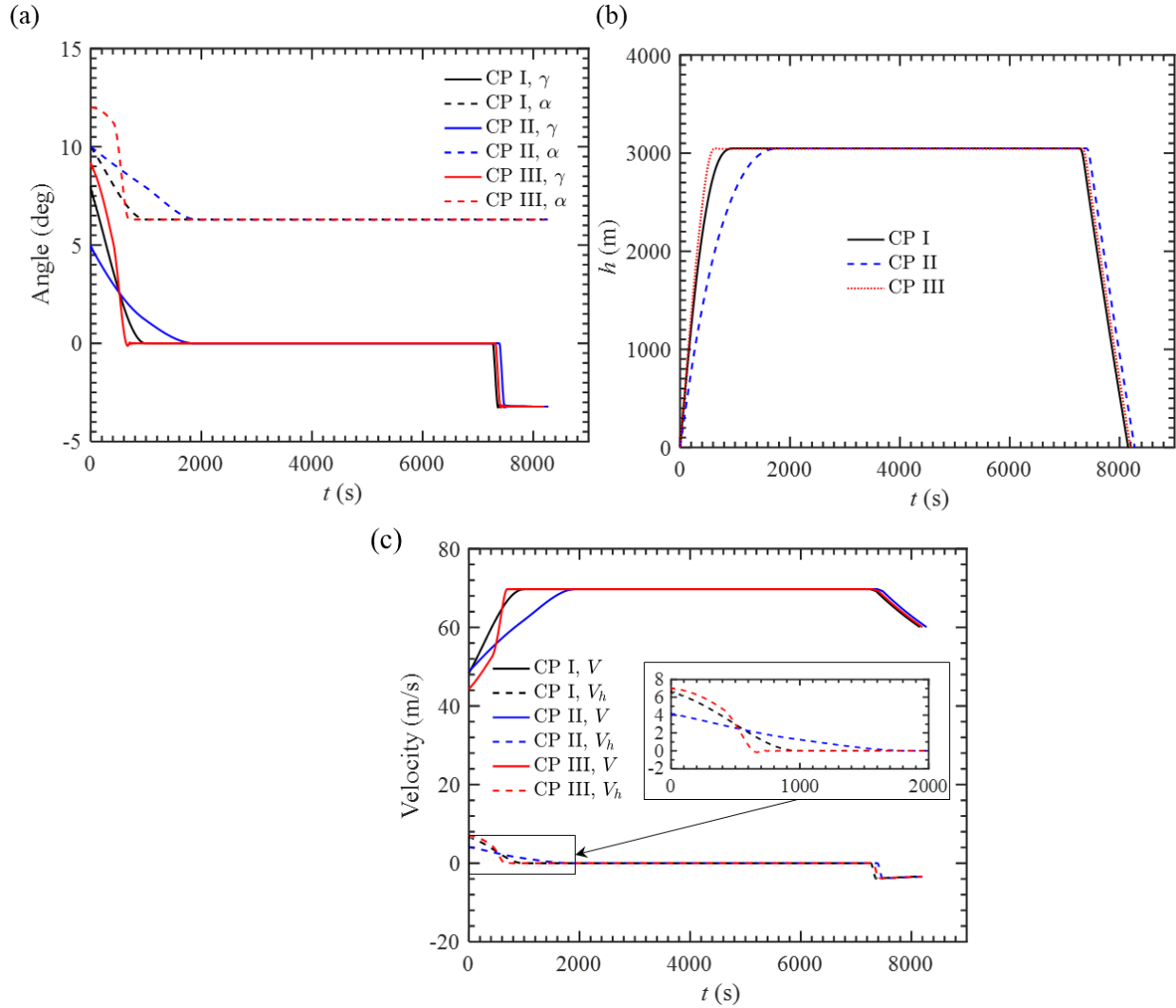


Fig. 10 (a) Angle of attack and flight path angle, (b) altitude, and (c) true airspeed and rate of climb versus flying time for different climb profiles under variable motor efficiency.

The motor shaft power P and energy consumption E are plotted in Fig. 11(a) and 11(b), respectively. For different climb profiles, there are significant differences of the transient power consumption during the climb as shown in Fig. 11(a). This is ascribed to the different control variables. The larger flight path angle for CP III in Fig. 10(a) leads to a higher rate of climb as well as higher power demand. As the cruise altitude and descent policy are the same for all mission profiles, P is similar during the cruise and descent phase as the cruise altitude remains the same. In terms of energy consumption in Fig. 11(b), it is found that the smaller average rate of climb results in lower energy consumption due to the lower P (Fig. 11(a)) and higher η_m (Fig. 3) as $\eta_m = \eta_m(\tau/\tau_0) = \eta_m(P/P_0)$. Here, P_0 is the motor power during cruise. The total E is slightly different owing to the different energy consumption during the climb phase. This aligns with our previous discussion in Sec. 5.1.

Overall, the predicted E , and t_f , and P_{max} are calculated in Table 5. The predicted values of t_f are similar for all cases since the cruise speed or altitude is the same. P_{max} shows the largest difference for different climb profiles since the initial angle of attack and flight path angle settings are very different as seen from Fig. 10(a). The relative total E or energy consumption excess in reference to that of CP I under constant η_m (case 7), namely ΔE , is illustrated in Fig. 12. For cases with constant motor η_m , it is interesting to note that the differences in E for different climb profiles are very small. From Eq. (27), the work done by the thrust is approximate to that of the gravity and drag. Since the gravity is conservative force, the final work done by the thrust will be equal to that of the drag. The work done by drag depends on the AEA trajectory whose length is equal to the area enclosed by the velocity curve and $y = 0$ axis in Fig. 10(c). It is seen that the enclosed areas are approximately the same for CP I, CP II, and CP III, resulting in similar values of E . The differences of E become obvious with a maximum value of ΔE up to 16 kWh (2.8% of the total energy consumption in case 7) as η_m is a function of P as shown in Fig. 12. It is noticeable that higher rate of climb results in higher energy consumption due to the average lower η_m as explained earlier.

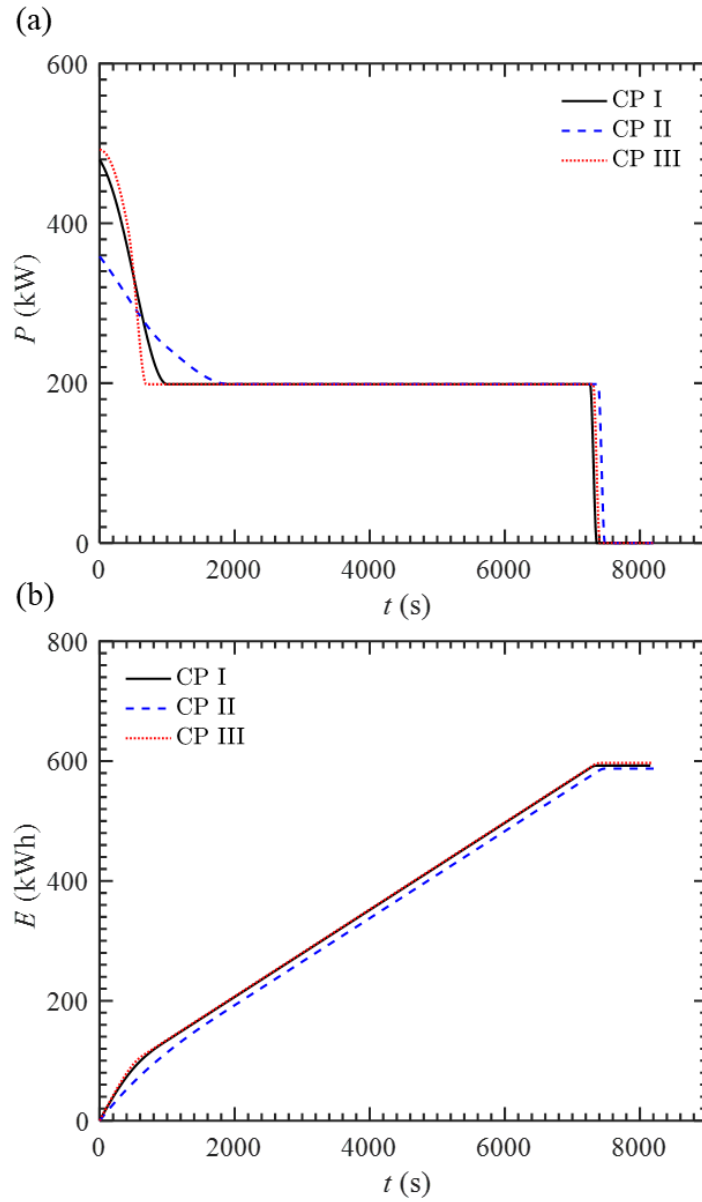


Fig. 11 (a) Motor shaft power and (b) energy consumption versus flying time for different climb profiles under variable motor efficiency.

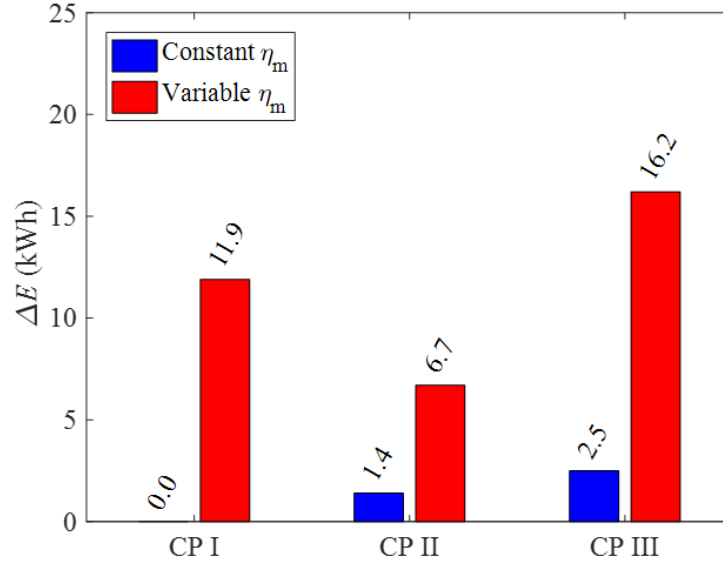


Fig. 12 Excess of total energy consumption for different climb profiles.

6. Conclusion

In this study, a 3DoF model and improved AM are proposed for predicting the flight range R , energy consumption E , flight time t_f , and maximum power of electric motor P_{max} of AEA corresponding to an electrified Cessna Caravan. The accuracies of improved AM along with the baseline AM are evaluated in comparison to the 3DoF model under different mission profiles and efficiencies of electric propulsion system for a mission resembling a Cessna Caravan. For the same flight range, the maximum errors of E and t_f predicted by AM relative to the 3DoF model are within 17% and 36%, respectively, while those by the improved AM are 5% and 8%. The baseline AM is also observed to give the poorest prediction of P_{max} with errors up to 85% while the errors of P_{max} by improved AM could be less than 4%. Further studies of R as a function of $\rho_{E,b}$, $\rho_{P,m}$, and number of passengers using the improved AM suggest that the electrification of regional short-haul flights with range less than 522 km is possible for the next ten years with the near-term battery and motor technology. In addition, R is found to be more sensitive to $\rho_{E,b}$ and payload. Finally, a sensitivity study of AEA energy consumption against different climb profiles is presented using the 3DoF model with constant (ideal) or variable (practical) η_m . For constant η_m , the differences in E for different climb profiles are less than 3 kWh (0.5% of the total energy consumption). However, the differences in E become more significant with a maximum value up to 16 kWh (2.8% of the total energy consumption) when the motor efficiency is modeled as a function of P . Since the battery energy storage is closely related to the AEA weight and cost, this study suggests that trajectory optimization conducted via low-cost algebraic models could lower the cost, improve the performance, and accelerate the design of AEA systems.

Acknowledgments

The present study was conducted with financial support from magniX.

References

- [1] Kozlova, M., Nykänen, T., & Yeomans, J. S. (2022). Technical Advances in Aviation Electrification: Enhancing Strategic R&D Investment Analysis through Simulation Decomposition. *Sustainability*, 14(1), 414.
- [2] Chuck, C. (Ed.). (2016). *Biofuels for Aviation: Feedstocks, Technology and Implementation*. Academic Press.
- [3] Ribeiro, R. F. G., Trapp, L. G., & Lacava, P. T. (2021). Economical Aspects of Aircraft Propulsion Electrification. In *2021 AIAA/IEEE Electric Aircraft Technologies Symposium (EATS)* (pp. 1-18). IEEE.
- [4] Buticchi, G., Wheeler, P., & Boroyevich, D. (2022). *The More-Electric Aircraft and Beyond*. Proceedings of the IEEE.
- [5] Schettini, F., Denti, E., & Di Rito, G. (2017). Development of a Simulation Platform of All-Electric Aircraft On-Board Systems for Energy Management Studies. *The Aeronautical Journal*, 121(1239), 710-719.
- [6] Brdnik, A. P., Kamnik, R., Marksel, M., & Božičnik, S. (2019). Beginning Steps of the Electrification of Commercial Passenger Aircraft Transport. In *European Transport Conference*.
- [7] Schäfer, A. W., Barrett, S. R., Doyme, K., Dray, L. M., Gnadt, A. R., Self, R., ... & Torija, A. J. (2019). Technological, Economic and Environmental Prospects of All-Electric Aircraft. *Nature Energy*, 4(2), 160-166.
- [8] Viswanathan, V., & Knapp, B. M. (2019). Potential for Electric Aircraft. *Nature Sustainability*, 2(2), 88-89.
- [9] Nagy, A. (2019). Electric Aircraft-Present and Future. *Production Engineering Archives*, 23(23), 36-40.
- [10] Schefer, H., Fauth, L., Kopp, T. H., Mallwitz, R., Friebe, J., & Kurrat, M. (2020). Discussion on Electric Power Supply Systems for All Electric Aircraft. *IEEE access*, 8, 84188-84216.
- [11] Barzkar, A., & Ghassemi, M. (2020). Electric Power Systems in More and All Electric Aircraft: A Review. *IEEE Access*, 8, 169314-169332.
- [12] Thapa, N., Ram, S., Kumar, S., & Mehta, J. (2021). All Electric Aircraft: A Reality on Its Way. *Materials Today: Proceedings*, 43, 175-182.
- [13] Clarke, M. A., & Alonso, J. J. (2023). Forecasting the Operational Lifetime of Battery-Powered Electric Aircraft. *Journal of Aircraft*, 60(1), 47-55.
- [14] Hull, D. G. (2007). *Fundamentals of Airplane Flight Mechanics (Vol. 19)*. Berlin: Springer.
- [15] Carretero, J. G. H., Nieto, F. J. S., & Cordón, R. R. (2013, May). Aircraft Trajectory Simulator Using a Three Degrees of Freedom Aircraft Point Mass Model. In *Proceedings of the 3rd International Conference on Application and Theory of Automation in Command and Control Systems* (pp. 114-117).
- [16] Aboelezz, A., Hassanalian, M., Desoki, A., Elhadidi, B., & El-Bayoumi, G. J. A. S. (2020). Design, Experimental Investigation, and Nonlinear Flight Dynamics with Atmospheric Disturbances of a Fixed-Wing Micro Air Vehicle. *Aerospace Science and Technology*, 97, 105636.
- [17] Allerton, D. (2009). *Principles of Flight Simulation (Vol. 27)*. John Wiley & Sons.

- [18] Giannakakis, P., Laskaridis, P., Nikolaidis, T., & Kalfas, A. I. (2015). Toward a Scalable Propeller Performance Map. *Journal of Propulsion and Power*, 31(4), 1073-1082.
- [19] Rivière, N., Volpe, G., Villani, M., Fabri, G., Di Leonardo, L., & Popescu, M. (2019, May). Design Analysis of a High Speed Copper Rotor Induction Motor for a Traction Application. In *2019 IEEE International Electric Machines & Drives Conference (IEMDC)* (pp. 1024-1031). IEEE.
- [20] Farhad, S., & Nazari, A. (2019). Introducing the Energy Efficiency Map of Lithium-Ion Batteries. *International Journal of Energy Research*, 43(2), 931-944.
- [21] Plett, G. L. (2015). *Battery management systems, Volume I: Battery modeling (Vol. 1)*. Artech House.
- [22] Plett, G. L. (2015). *Battery Management Systems, Volume II: Equivalent-Circuit Methods*. Artech House.
- [23] Traub, L. W. (2011). Range and Endurance Estimates for Battery-Powered Aircraft. *Journal of Aircraft*, 48(2), 703-707.
- [24] Ma, S., Jiang, M., Tao, P., Song, C., Wu, J., Wang, J., ... & Shang, W. (2018). Temperature Effect and Thermal Impact in Lithium-Ion Batteries: A Review. *Progress in Natural Science: Materials International*, 28(6), 653-666.
- [25] Ang, A. W. X., Gangoli Rao, A., Kanakis, T., & Lammen, W. (2019). Performance Analysis of an Electrically Assisted Propulsion System for a Short-Range Civil Aircraft. *Proceedings of the Institution of Mechanical Engineers, Part G: Journal of Aerospace Engineering*, 233(4), 1490-1502.